RSC Advances

PAPER

View Article Online
View Journal | View Issue

Cite this: *RSC Adv.*, 2026, **16**, 13243

Two-dimensional Ruddlesden–Popper perovskite microcrystal photodetectors with high detectivity for ultra-weak light detection

Yunuan Wang, * Yanping Ma, Jianxiang Liu and Shaopeng Li

Received 27th November 2025
Accepted 13th February 2026

DOI: 10.1039/d5ra09159d

rsc.li/rsc-advances

Strong light absorption capabilities, excellent semiconductor properties, and enhanced humidity and light stability have led to the rapid development of two-dimensional (2D) organic–inorganic metal halide perovskites in the field of light detection. However, so far, the research on weak light detection of 2D perovskite is insufficient, and its detection limit needs to be further broken. Here, high-quality ($C_6H_5CH_2CH_2NH_3$, PEA)$_2PbBr_4$ perovskite single crystals with low defect density are prepared. Lateral photodetectors based on this perovskite single crystal demonstrate stable photoresponse under ultra-weak ultraviolet illumination. The very low dark current of 4.75×10^{-11} A provides a low-noise baseline that is essential for achieving high detectivity under weak light conditions. Even at an optical power density as low as 2.47 nW cm^{-2}, the device exhibits a responsivity of 19.23 A W^{-1}. The corresponding gain and specific detectivity reach 58.80 and 1.22×10^{14} Jones, respectively. These results confirm the suitability of 2D perovskite single crystals for ultra-weak light photodetection.

Introduction

With the continuous development of science and technology, people have higher and higher requirements for material and spiritual life and thus have higher demands for photodetectors that are widely used in medicine,[1] biological monitoring,[2,3] military,[4] and other fields.[5–7] Especially, weak light detectors, although they play a vital role in astronomical observations,[8] non-destructive material analysis,[9] night vision,[10] and other fields,[11] when they detect weak light signals, they are often affected by background light, dark noise from photodetectors, and noise from amplification circuits, which makes it difficult to detect weak light signals.[12] At present, commercialized weak light detection devices are mainly silicon-based avalanche photodetectors[13] and photomultiplier tubes[14] with good stability and low noise. However, due to limitations in technical characteristics, the high manufacturing cost of these devices and the complexity of their manufacturing processes have greatly hindered their development in the direction of low cost, functionality, and digitization. In comparison, perovskite materials have the characteristics of low cost and simple preparation methods.[15,16] High-quality perovskite crystals can be obtained at room temperature.[17] Coupled with their long carrier diffusion length, high carrier mobility, and large optical absorption coefficient, they are considered to be some of the candidate materials for weak light detectors.[18–20]

Currently, perovskite-based photodetectors have made some progress in weak light detection. For example, Xing *et al.* prepared flexible self-powered weak light detectors based on a three-dimensional (3D) $CsPbBr_3$ film.[21] When the light intensity is 0.01 mW cm^{-2}, the detectivity (D^*) is as high as 8.11×10^{13} Jones. On the other hand, Liu *et al.* prepared a vertical structure ultraviolet (UV) photodetector based on 3D $CH_3NH_3PbCl_3$ perovskite film.[22] At a light intensity of 0.6 μW cm^{-2}, the D^* is calculated to be 7.08×10^{11} Jones. Compared with 3D perovskites, two-dimensional (2D) organic–inorganic hybrid perovskites have higher humidity stability because of their larger hydrophobic organic groups such as PEA^+ ($C_6H_5C_2H_4NH_3^+$) and BA^+ ($C_4H_9NH_3^+$).[23,24] This stability makes them particularly appealing for various applications where environmental conditions might vary.

Layered 2D organic–inorganic hybrid perovskites, characterized by a structure of alternating inorganic framework layers and various organic cation layers, have significantly broadened the system of perovskite materials.[25,26] Large organic cations acting as spacers can cut bulk perovskites into 2D materials, resulting in unique quantum well structures and optoelectronic properties.[27] Its good semiconductor properties and excellent light absorption properties make it popular in short-wavelength light detection.[28,29] Currently, 2D perovskites have also made some promising progress in UV weak light detection. For example, Li *et al.* designed a self-powered photodetector based on the PEA_2SnI_4 film/Si nanowire vertical heterojunction.[19] When the light intensity is 4.6 nW cm^{-2}, the on/off ratio of the device is as high as 18.6, and the responsivity (R) and D^* are 42.4 mA W^{-1} and 8×10^{11} Jones, respectively. Zhang *et al.* reported a photodetector based on

Institute of Automation, Qilu University of Technology (Shandong Academy of Sciences), Jinan 250014, P. R. China. E-mail: yunuanwang@163.com

centimeter-sized ($C_3H_7NH_3$, PA)$_2$PbBr$_4$ perovskite single crystal for 405 nm short wavelength detection.[30] When the light intensity is 20 nW cm^{-2}, D^* is 6.08 × 10^{12} Jones and R is 91.2 mA W^{-1}. Despite this, research on 2D perovskite photodetectors with weak light detection capabilities is just in its infancy and remains less explored compared with the well-established research on 2D perovskite solar cells. Therefore, photodetectors based on 2D hybrid perovskite materials still have huge development space in weak light detection.

Herein, a micron-level high-quality 2D Ruddlesden–Popper type (PEA)$_2$PbBr$_4$ organic–inorganic hybrid perovskite single crystal was prepared. A lateral photodetector with a low detection limit and high sensitivity was manufactured based on this crystal. At an extremely low light intensity of 2 nW cm^{-2}, the device still exhibits a significant photoresponse, benefiting from the high quality of the single crystal and the low dark current of the photodetector. The low detection limit falls almost near the minimum value for short-wavelength light photodetectors based on 2D hybrid perovskites. This work has the potential to promote the application of 2D organic–inorganic hybrid perovskite materials in high-performance weak short-wavelength light detection.

Results and discussion

The right panel in Fig. 1a denotes the schematics of the crystal structure of 2D (PEA)$_2$PbBr$_4$ perovskite (PEA)$_2$PbBr$_4$ perovskite is composed of organic layers and inorganic framework layers alternately stacked in the direction perpendicular to the plane. The organic layer is composed of organic cationic PEA$^+$, while the inorganic framework layer is constructed of [PbBr$_4$]$^{2-}$ octahedrons connected *via* common vertices. The left panel in Fig. 1a sketches the energy band structure of 2D (PEA)$_2$PbBr$_4$ perovskite. Due to the significant disparity between the band gap of the [PbBr$_4$]$^{2-}$ inorganic layer and the highest occupied molecular orbital (HOMO)-lowest unoccupied molecular orbital (LUMO) gap of the PEA$^+$ organic layer, a natural type-I quantum well structure is formed. Here, the organic layer serves as a barrier, while the inorganic layer acts as a well. This arrangement results in a pronounced quantum confinement effect within the 2D (PEA)$_2$PbBr$_4$ perovskite.[31] In addition, the dielectric constants of the organic and inorganic layers in (PEA)$_2$PbBr$_4$ perovskites are 3.32 and 4.8 respectively.[32] The disparity in dielectric constants makes it difficult for the organic layer to shield the Coulomb interaction between electrons and holes in the quantum well, thus producing a strong dielectric confinement effect in 2D (PEA)$_2$PbBr$_4$ perovskite.[33] Due to the dual influences of quantum confinement and dielectric confinement effects, the interaction of electron–hole pairs in the potential well layer of (PEA)$_2$PbBr$_4$ perovskite is enhanced, therefore, the exciton binding energy of the (PEA)$_2$PbBr$_4$ perovskite with type-I quantum well structure is large and can usually reach hundreds of millielectron volts (meV).[34]

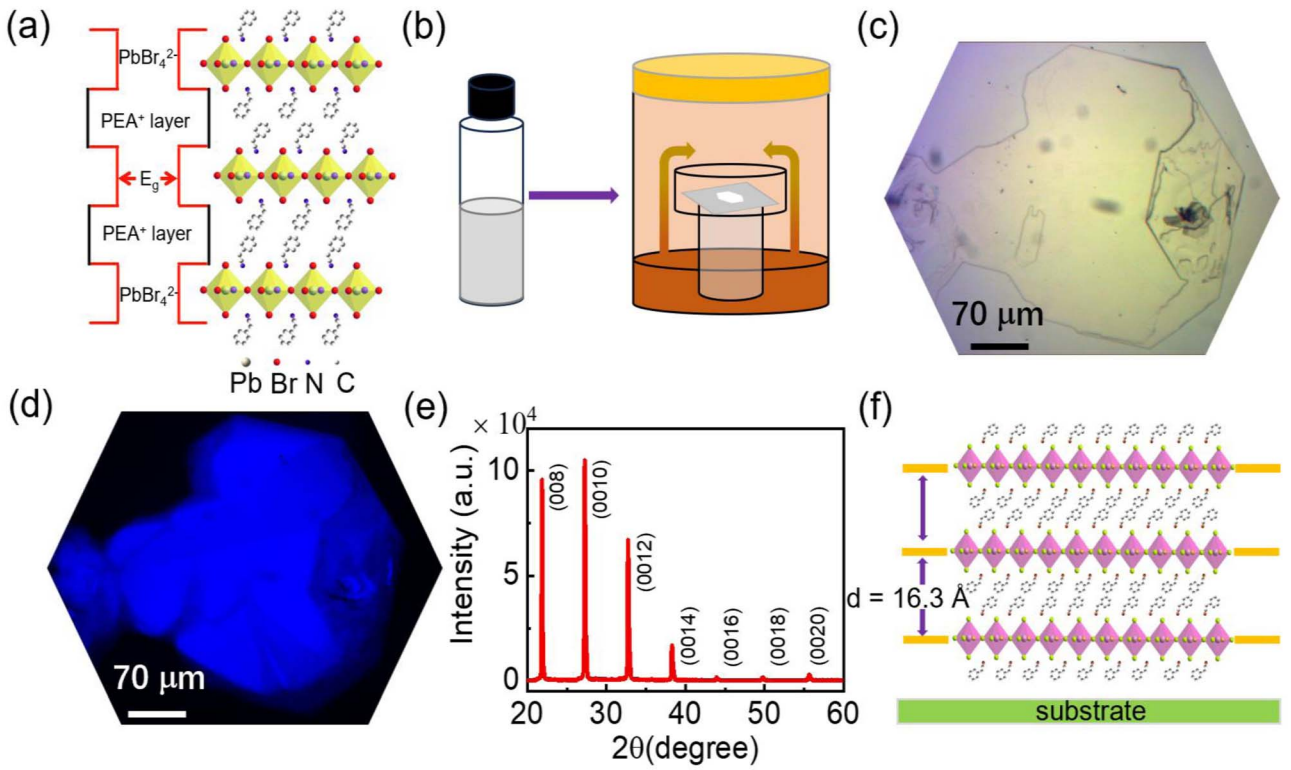

Fig. 1 (a) The crystal structure of 2D (PEA)$_2$PbBr$_4$ perovskite along with its energy band structure. (b) Schematic diagram of synthesizing (PEA)$_2$PbBr$_4$ perovskite single crystal by the anti-solvent vapor-assisted method (ASV). (c) and (d) optical and corresponding fluorescence micrographs of the as-grown (PEA)$_2$PbBr$_4$ perovskite single crystal. (e) and (f) X-ray diffraction (XRD) pattern and the diffraction plane arrangement of the obtained 2D (PEA)$_2$PbBr$_4$ perovskite.

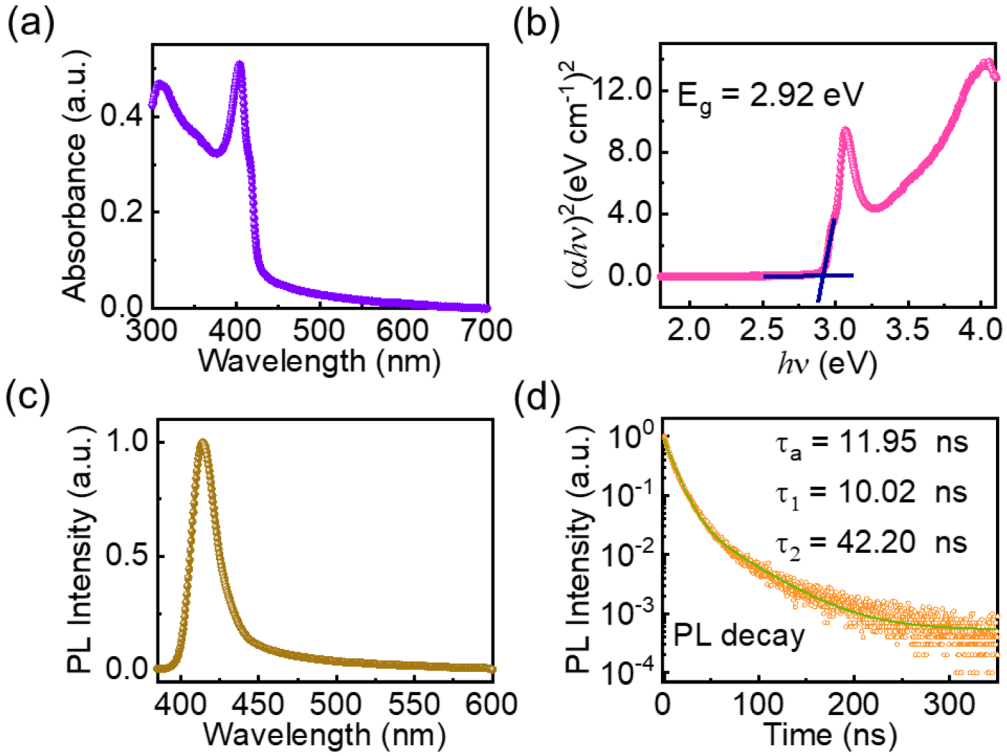

Fig. 2 (a) and (b) Steady-state UV-vis absorption spectra and Tauc plot of as-grown $(PEA)_2PbBr_4$ perovskite single crystal. (c) and (d) room temperature steady-state and time-resolved PL spectra of the $(PEA)_2PbBr_4$ single crystal on glasses.

In this work, high crystalline quality $(PEA)_2PbBr_4$ perovskite single crystals were obtained by an anti-solvent vapor-assisted method (ASV), as shown in Fig. 1b. Specifically, in an environment with a humidity of 30%, a certain amount of PEABr and $PbBr_2$ powders were dissolved in the benign solvent *N*,*N*-dimethylformamide (DMF) to obtain a perovskite precursor solution. Then, drop an appropriate amount of the precursor solution on the substrate and place it in an atmosphere of anti-solvent dichloromethane (CH_2Cl_2) for 12 h to obtain a high-quality $(PEA)_2PbBr_4$ perovskite single crystal. Fig. 1c and d depict the optical and fluorescence microscope images of a $(PEA)_2PbBr_4$ perovskite single crystal. The crystal exhibits a platelet morphology with a width of ~350 μm and a length exceeding 440 μm. According to the measurement results of the profilometer, it is found that the thickness of the crystal is about 1 μm.

In order to characterize the crystal structure of the $(PEA)_2PbBr_4$ perovskite single crystal, the XRD measurement is executed, and its result is displayed in Fig. 1e. It is evident that only the diffraction peaks of the (00l, l = 8, 10, 12, …, 20) plane at 21.8, 27.2, 32.8, 38.3, 44.0, 49.7, and 55.6 are observed. The exclusive presence of out-of-plane (00l) reflections indicates that the crystal is highly oriented with its *c*-axis perpendicular to the substrate (Fig. 1f). This preferential orientation is typical for layered Ruddlesden–Popper (RP) perovskites and is directly related to their anisotropic charge transport behavior. Similar correlations between vertical crystallographic alignment and anisotropic photoconductivity have been reported in solution-processed 2D lead-halide perovskite films fabricated by bar (blade) coating methods.[35] In addition, the observed high-order diffraction peaks indicate that the perovskite obtained based on method ASV has higher crystalline quality. Using Bragg's Law, $2d\sin\theta = n\lambda$, the long cell dimension along the *c*-axis is calculated to be 16.3 Å based on the fourth-order diffraction peak (2θ = 21.8) corresponding to the diffraction of the (008) plane. Therefore, the interlayer spacing of the $(PEA)_2PbBr_4$ perovskite single crystal along the *c*-axis direction is confirmed to be 16.3 Å, which aligns with previously reported values in the literature.[36]

To study the optical properties of as-grown 2D $(PEA)_2PbBr_4$ perovskite single crystals, steady-state ultraviolet-visible (UV-vis) absorption and photoluminescence (PL) spectroscopy measurements were performed. Among them, the UV-vis absorption spectrum is depicted in Fig. 2a, showing an obvious absorption cutoff at 428 nm. Moreover, owing to the large exciton binding energy in 2D perovskites resulting from strong quantum and dielectric confinement effects, a sharp and strong absorption peak caused by exciton absorption at the band edge is displayed at ~404 nm even at room temperature. For $(PEA)_2PbBr_4$ perovskite, the organic layer PEA^+ is transparent in the visible range, so the exciton absorption is generated by excitons from the inorganic layer $[PbBr_4]^{2-}$. The optical band gap (E_g) of $(PEA)_2PbBr_4$ perovskite single crystal can be obtained by the formula $(\alpha h\nu)^2 = k(h\nu - E_g)$. In the equation, α represents the optical absorption coefficient of the material, h and ν are Planck constant and the frequency of the incident photon respectively, and k is a constant.[37] Fig. 2b denotes the

variation trend of $(\alpha h\nu)^2$ with perovskite photon energy $h\nu$, E_g of 2.92 eV is obtained by fitting. Theoretical calculations reveal that the E_g of $(PEA)_2PbBr_4$ is mainly contributed by Pb (5 s) and Br (4p) orbitals, which is conducive to the transition of electrons under illumination.[30]

Fig. 2c depicts the PL spectrum of as-grown $(PEA)_2PbBr_4$ perovskite single crystal under the excitation of 369 nm wavelength light. A sharp emission peak with a full width at half maximum (FWHM) of ~13 nm appears at ~413 nm, which corresponds to the exciton absorption peak at ~404 nm, and a 9 nm red shift occurs as a result of the Stokes shift due to exciton–phonon scattering.[38] The narrow bandwidth of the PL spectrum illustrates the high color purity of as-grown perovskite single crystal, which is a key performance metric in luminescence applications. It is worth noting that the PL spectrum is not symmetrical and has a tail in the low energy direction. This phenomenon may be due to the significant quantum and dielectric confinement effects in the 2D $(PEA)_2PbBr_4$ perovskite, which results in the existence of multiple exciton states, the coupling of excitons and phonons, and the radiative recombination of trap states.[39,40]

To study the carrier recombination dynamics of $(PEA)_2PbBr_4$ perovskite single crystals, time-resolved photoluminescence (TRPL) spectroscopy was performed. The measurement result shown in Fig. 2d indicates that the TRPL spectrum of as-grown $(PEA)_2PbBr_4$ perovskite single crystal has a biexponential decay feature. Therefore, by fitting it with the formula $y = A_{exp}(-t/\tau_1) + B_{exp}(-t/\tau_2)$,[41] the fast component lifetime τ_1 and the slow component lifetime τ_2 are 10.02 and 42.20 ns respectively. Different recombination mechanisms on the surface and in the bulk of $(PEA)_2PbBr_4$ perovskite single crystal give rise to this fast and slow time component.[42] The fast component arises from non-radiative recombination caused by defects, while the slow component comes from the radiative recombination of photogenerated carriers.[43] Through calculation, an average fluorescence lifetime of 11.95 ns was obtained, which is significantly higher than that of the same perovskite polycrystalline thin film ($\tau \approx 0.62$ ns),[44] and also higher than the value of this perovskite single crystal previously reported in the literature ($\tau_1 = 1.23$ ns, $\tau_2 = 5.31$ ns).[42] The longer fluorescence lifetime demonstrates an extended carrier lifetime, which benefits from the low trap state density of as-grown $(PEA)_2PbBr_4$ single crystal.[42] For photodetectors, this key characteristic promotes the transmission of photogenerated carriers and reduces dark current, thereby enhancing device performance.[30]

In addition, for 2D $(PEA)_2PbBr_4$ perovskite, carriers are mainly limited to the 2D plane. The PEA^+ organic cations hinder the transmission of carriers in the *c*-axis direction. In the ab crystal plane, the $[PbBr_4]^{2-}$ inorganic framework not only has good carrier transport properties but also has a high light absorption coefficient.[30] Therefore, a lateral photodetector with two indium tin oxide (ITO) planar electrodes was constructed, where the $(PEA)_2PbBr_4$ single crystal bridges the pre-patterned ITO channel to enable in-plane carrier transport. The structural schematic diagram of the device and the photoresponse measurement mechanism are depicted in Fig. 3a. In this device

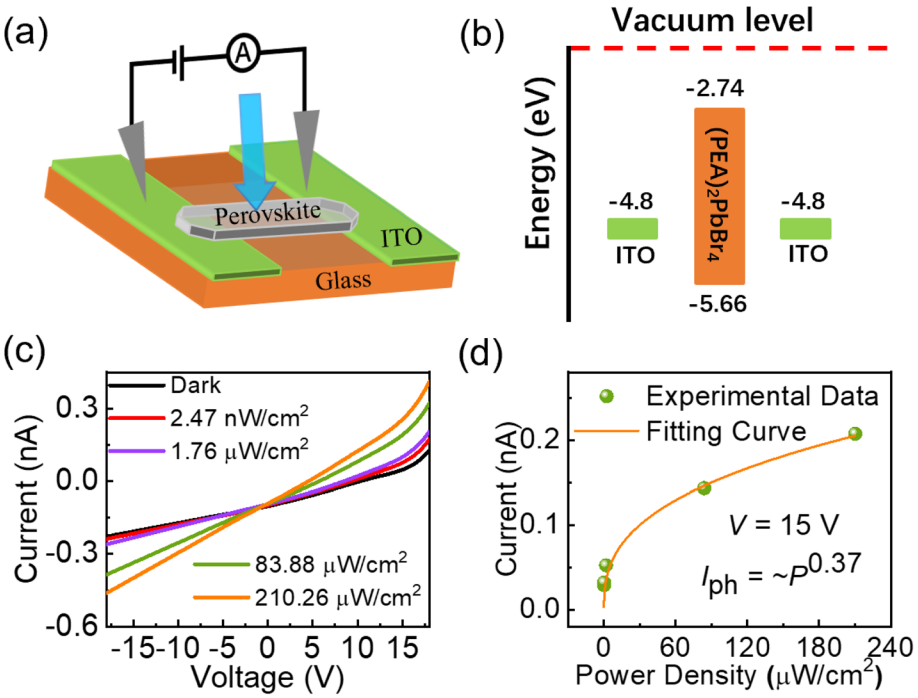

Fig. 3 (a) The structural schematic diagram of the photodetector accompanied by the photoresponse measurement mechanism. (b) The energy level structure of the $(PEA)_2PbBr_4$ perovskite combined with the work function of two ITO electrodes. (c) The current–voltage curves of the device in the dark and under 405 nm light irradiation with various intensities. (d) When the bias voltage is 15 V, the functional relationship between photocurrent and optical power density.

architecture, the $(PEA)_2PbBr_4$ single crystal is placed on top of the pre-patterned ITO planar electrodes, forming a lateral conduction channel. Carrier transport therefore mainly occurs along the in-plane (ab) direction of the crystal rather than across the electrode–perovskite interface. In this configuration, the role of ITO is primarily to provide a stable and low-resistance carrier collection pathway, while the transport behavior and dark current characteristics are governed by the intrinsic anisotropic charge transport nature of the 2D RP crystal itself.[45]

Two ITO electrodes construct a channel with a length of 87 μm and a width of 1 mm. In this work, the width of the single crystal is smaller than that of the channel and therefore does not completely cover the channel region. Consequently, the effective photosensitive area is determined by the overlap between the single crystal and the channel, which is 87 μm × 700 μm, corresponding to 6.09×10^{-4} cm^2. This effective area was used in all calculations of responsivity and specific detectivity in this study. Fig. 3b illustrates the energy level structure of the $(PEA)_2PbBr_4$ perovskite single crystal and the work function of electrode ITO.

The photoresponse characteristics of the photodetector were obtained by measuring the current–voltage (*I–V*) curves of the device in the dark and under 405 nm light irradiation with different intensities (Fig. 3c). When the light intensity or the applied voltage is constant, the current increases as the intensity of the incident light or the applied voltage increases. When there are no light irradiation and the bias voltage is 15 V, the dark current (I_{dark}) is 4.75×10^{-11} A, indicating a low-noise baseline of the device. Dark current values reported in the literature are highly sensitive to bias voltage and device geometry. Representative reports for 2D RP perovskite single-crystal photodetectors include $(PEA)_2PbI_4$ (3.06×10^{-12} A at 5 V),[46] $(BA)_2PbBr_4$ ($\sim 10^{-10}$ A at <1 V),[47] and previously reported $(PEA)_2PbBr_4$ single crystals (2.81×10^{-12} A at 10 V).[30]

The relatively low dark current observed in this device is closely related to the intrinsic structural characteristics of the 2D RP perovskite. The bulky PEA^+ spacer cations form hydrophobic and electronically insulating organic layers between the inorganic slabs, introducing a substantial transport barrier along the out-of-plane direction.[45] Such a layered architecture is known to strongly restrict interlayer carrier conduction and is therefore favorable for reducing background leakage current in photodetectors. This understanding is consistent with previous studies on layered RP perovskite single crystals, where intrinsically low dark current densities have been widely reported due to limited out-of-plane conductivity. In particular, *para*-F-substituted $(PEA)_2PbX_4$ single crystals have shown, through space-charge-limited current (SCLC) analysis, trap densities several orders of magnitude lower than those of conventional 3D perovskites, which correlates with suppressed dark current and enhanced device sensitivity.[48] This suppression of leakage current originates from the intrinsic layered crystal structure rather than from the electrode material, since the lateral ITO configuration does not introduce additional carrier injection pathways along the out-of-plane direction. In addition, the electronically insulating organic spacer layers impose an additional transport barrier that suppresses trap-assisted tunneling and thermally activated carrier generation under dark conditions. Similar design strategies employing functional organic groups to block parasitic conduction pathways have also been demonstrated in perovskite optoelectronic nanodevices, highlighting the broader applicability of this structural principle for achieving low-noise photodetection.[49]

It is worth noting that the measured dark *I–V* curve exhibits a offset around zero bias and does not strictly pass through the origin. This behavior is attributed to the slight asymmetry of the practical lateral metal–semiconductor–metal device configuration. The $(PEA)_2PbBr_4$ microcrystal does not fully cover the ITO channel, and the two electrode–crystal contacts are therefore not perfectly identical. Such contact asymmetry can introduce a built-in potential and lead to near-zero-bias offsets in the *I–V* characteristics.[50] In addition, metal halide perovskites are mixed ionic–electronic conductors, and the redistribution of mobile ions under an external electric field may give rise to scan-direction-dependent hysteresis and a remanent internal field, which further contributes to the observed offset.[51,52] Therefore, the sign of the current close to zero bias reflects the measurement convention and bias history and does not affect the evaluation of device sensitivity when absolute current values and net photocurrent are considered. All *I–V* curves were recorded using a voltage sweep from positive to negative bias at a fixed scan rate.

The relatively low dark current provides a reliable foundation for high-performance photodetection. With a fixed bias voltage, when the light intensity is 210.26 μW cm^{-2}, the current (I_{light}: current under illumination) rises to 2.55×10^{-10} A, corresponding to an on/off ratio defined as $|I_{light}|/|I_{dark}|$ of 5.4. Importantly, even at an ultra-low light intensity of 2.47 nW cm^{-2}, the device still exhibits a distinguishable photocurrent with an on/off ratio of 1.61. This behavior demonstrates that the photodetector can respond to light at the nW cm^{-2} level. Such sensitivity primarily originates from the intrinsically suppressed dark current and the anisotropic charge-transport characteristics of the 2D $(PEA)_2PbBr_4$ crystal structure.

To further demonstrate the capability and advantages of the device in weak-light detection, the photocurrent I_{ph} ($I_{ph} = I_{light} - I_{dark}$) is presented as a function of optical power density *P*, as shown in Fig. 3d. They follow the formula I_{ph}–P^k, where the empirical value *k* is determined by the response of I_{ph} to *P*.[53] The larger the *k* value, the more sensitive the photocurrent is to light intensity, and the steeper the corresponding I_{ph} – *P* curve. In practical applications, the *k* value should be equal to or close to 1. By fitting, a *k* of 0.37 is obtained, which is much less than 1. It is related to the processes of electron–hole generation, recombination, and trapping in $(PEA)_2PbBr_4$ perovskite single crystal.[54,55] It is worth noting that when the optical power density is very small, the fitting curve is very steep, and as the light intensity increases, the growth rate of the photocurrent becomes slower, proving that the as-fabricated device is more sensitive to weak light, suggesting that it has great potential in weak light detection.

In addition, responsivity (*R*), photoconductive gain (*G*) and specific detectivity (*D**), as important parameters of the photodetector, can also be used to evaluate the device's ability to

detect weak light.[53,56] The relationship between the incident light power and the device output signal is represented by R, which is defined as follows: $R = I_{ph}/(PS)$. Here, S is the effective area of the photodetector. G is the ratio of the number of majority carriers collected by the electrodes to the number of photons absorbed by the device per unit time. Therefore, G is expressed by the formula $G = I_{ph}hv/(eP)$, e signals the elementary charge. In addition, G can also be expressed as the ratio of the lifetime of the excess minority carriers (τ) to the transfer time of the majority carriers (τ_t) from one electrode to another ($G = \tau/\tau_t$). The specific detectivity D^*, which is usually used to evaluate the response ability of photodetectors to weak light signals, is expressed as follows: $D^* = I_{ph}\sqrt{S}/(P\sqrt{2el_{dark}})$.

Fig. 4a sketches the responsivity and gain of as-fabricated photodetector as a function of optical power density at a fixed bias voltage of 15 V. It is obvious that both R and G decrease as the incident optical power density increases. Therefore, the smaller the light intensity, the greater the values of R and G. When the optical power density is 2.47 nW cm^{-2}, R and G reach the maximum values of 19.23 A W^{-1} and 58.80. The G value far exceeds 1, indicating that in $(PEA)_2PbBr_4$ perovskite single crystal, the lifetime of photogenerated electrons is much longer than the time of hole transfer. Specifically, when the incident light intensity is not zero, an incident photon is absorbed by the photosensitive material $(PEA)_2PbBr_4$ perovskite, generating an electron–hole pair. Since the lifetime of photogenerated electrons is very long compared to the time it takes for holes to transfer from one electrode to another, when an external voltage is present, after the photogenerated holes reach the cathode, another hole will be injected from the anode to the $(PEA)_2PbBr_4$ perovskite material to ensure electrical neutrality. Holes drift from the anode to the cathode until the photogenerated electron recombines with the last excess hole, so G is greater than 1. What's more, G decreases as the light intensity increases as a result of trap saturation. In detail, as the light intensity increases, the defect states in the $(PEA)_2PbBr_4$ perovskite are gradually filled, causing the number of free carriers inside the perovskite material to gradually increase. The increased number of free carriers increases the probability of electron–hole recombination, so when the light intensity increases, the gain G decreases. Under a fixed light intensity of 2.47 nW cm^{-2}, the changes of R and G with bias voltage are shown in Fig. 4b. As the voltage continues to increase, both R and G increase. Therefore, when the voltage is 20 V, R and G reach the maximum of 36.54 A/W and 111.71.

Fig. 4c and d respectively reveal the variation pattern of the specific detectivity D^* with voltage and light intensity under the premise that the light intensity or voltage remains unchanged. Like R and G, within a certain range, D^* also increases with the increase of voltage and decreases with the increase of light intensity. When the incident light power density is 2.47 nW cm^{-2} and the voltage is 15 V, its value is as high as 1.22×10^{14} Jones (cm Hz$^{1/2}$ W^{-1}). It is not only significantly higher than the value of 7.08×10^{11} Jones for 3D $CH_3NH_3PbCl_3$ perovskite film

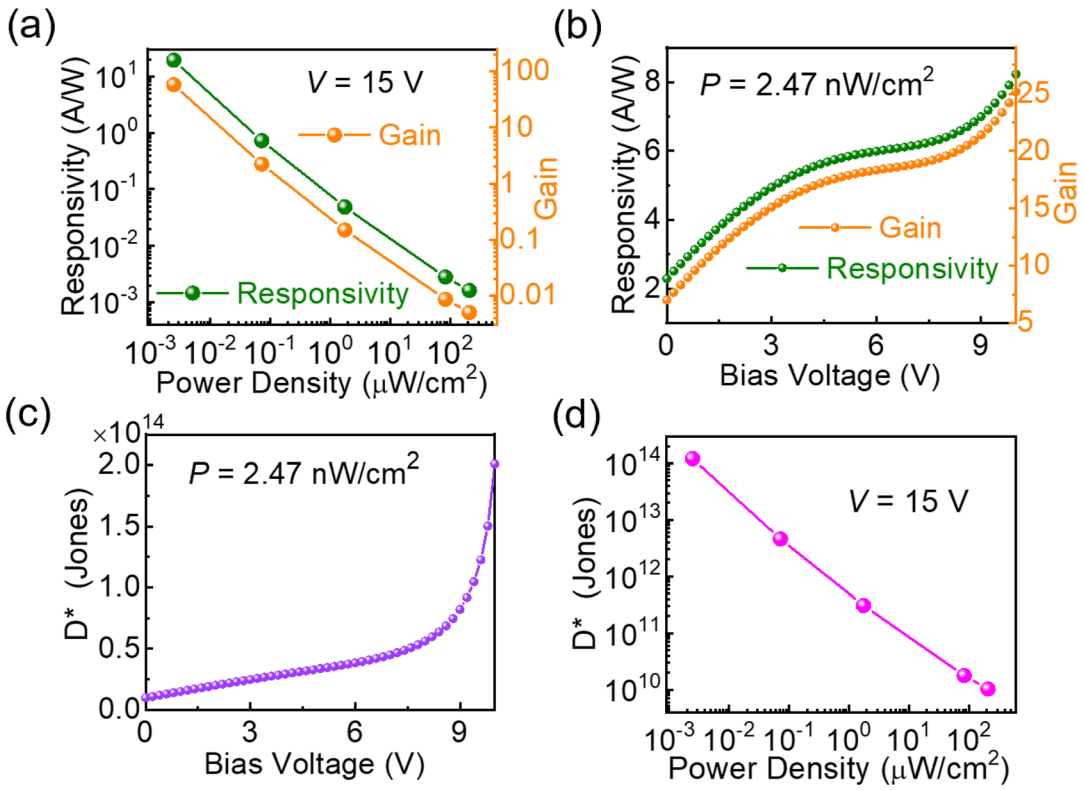

Fig. 4 (a) At a fixed voltage of 15 V, the responsivity R and gain G of as-fabricated photodetector under different incident light power densities. (b) At a fixed incident optical power density of nW cm^{-2}, the changes in the optical response and gain of the device to the applied bias voltage. (c) and (d) when the incident light intensity or bias voltage is constant, the specific detectivity D^* as a function of voltage or incident light intensity.

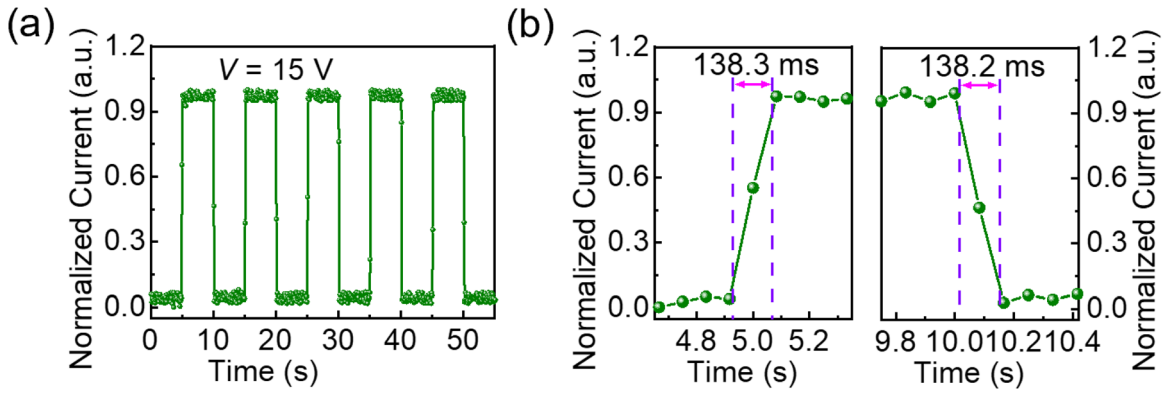

Fig. 5 (a) Optical switching behavior of the photodetector based on as-grown $(PEA)_2PbBr_4$ perovskite single crystal under 405 nm light irradiation at a voltage of 15 V. (b) The rise and decay characteristics of as-fabricated device.

photodetectors but also far exceeds the value of 6.02×10^{12} and 1.55×10^{13} Jones for devices based on the same perovskite single crystal with the same structure.[22,30,42]

Response time, which is related to the extraction of photogenerated carriers, is also a key parameter to evaluate the performance of photodetectors. Response time is mainly related to the extraction of light-generated carriers. The rise time (t_r) corresponds to the time required for the photocurrent to increase from 10% to 90% of its maximum value, while the decay time (t_f) represents the time for the photocurrent to decrease from 90% to 10%.[57] Fig. 5a denotes the time-resolved photoresponse of the as-fabricated photodetector under 10 V bias and 405 nm light irradiation, where the light pulse interval is set to 5 s. Five cycles of optical switching testing showed almost no change in the photocurrent of the device, proving that the photodetector has good stability and repeatability. The rise and decay characteristics of the device are shown in Fig. 5b with rise and decay times of 138.3 and 138.2 ms. The relatively long channel of the device results in a longer response time, but they are still within the common response time range for lateral photodetection based on perovskite single crystals.[5] It is worth emphasizing that the decay time of the as-fabricated device is not greater than the rise time, and there is no rising trend of current within 5 measurement cycles, which is since the as-grown perovskite single crystal has better crystal quality and less defect state density. It is precisely because of these that the as-fabricated device shows great advantages and good application potential in weak-light detection.

To further evaluate the environmental stability of the device, the as-fabricated photodetector was stored under ambient conditions with a relative humidity of approximately 60% for 8 days and then re-measured under identical testing conditions.

Table 1 Comparison of the key device parameters before and after aging under 60% relative humidity for 8 days, measured at a fixed bias of 15 V and an incident light intensity of 2.47 nW cm^{-2}

Aging time	R (A W^{-1})	D^* (Jones)	G
0 day	19.23	1.22×10^{14}	58.80
8 days	19.81	7.76×10^{13}	61.86

The detailed aging results are provided in Fig. S1–S4 in the SI. As shown in Fig. S1, at a bias voltage of 15 V, the dark current increases from 4.75×10^{-11} A to 1.24×10^{-10} A after aging. Fig. S2–S4 present the variations of photocurrent, responsivity, gain and specific detectivity with light intensity after aging. The key device parameters before and after aging at an incident light intensity of 2.47 nW cm^{-2} and a bias voltage of 15 V are summarized in Table 1. It can be observed that the responsivity (R) and gain (G) remain almost unchanged after aging, while the specific detectivity (D^*) shows a decrease. This reduction is mainly associated with the increase in dark current under humid conditions. Such behavior can be mainly attributed to moisture-assisted ionic migration, which induces weak self-doping effects and introduces additional background carriers in the perovskite single crystal.[58] Importantly, the nearly unchanged R and G indicate that the photogenerated carrier transport and collection processes in the $(PEA)_2PbBr_4$ single crystal are not significantly affected. These results demonstrate that the device maintains stable photoresponse capability under moderate humidity.

Conclusions

In summary, we used the anti-solvent vapor-assisted method to prepare 2D $(PEA)_2PbBr_4$ perovskite single crystal with high crystal quality and low defect state density. The crystal size is more than hundreds of microns. Lateral photodetectors fabricated from these single crystals demonstrate reliable photoresponse under ultra-weak light illumination at the nanowatt-per-square-centimeter level. The device shows a low dark current of 4.75×10^{-11} A, together with a responsivity of 19.23 A W^{-1}, a specific detectivity of 1.22×10^{14} Jones, and a gain of 58.8. These results highlight the suitability of 2D RP perovskite single crystals for ultra-weak light detection and provide useful insight into the role of intrinsic layered structure in suppressing background leakage current.

Experimental

Device fabrication

The specific steps of the antisolvent evaporation-assisted method to obtain high crystalline quality 2D $(PEA)_2PbBr_4$

perovskite single crystals have been given in previous reports.[56] Optical and fluorescence microscope images were recorded through the L3230 optical microscope. The XRD measurement was performed *via* a Bruker D8 X-ray diffractometer with Cu Kα radiation ($\lambda = 1.54$ Å). The UV-vis absorption spectrum and PL spectrum of as-grown 2D $(PEA)_2PbBr_4$ perovskite single crystal were measured by a spectrophotometer (UV-3101 PC, Shimadzu) and a Horiba Fluorolog system spectrometer respectively. Among them, the excitation wavelength used in PL measurement is 369 nm. The current–voltage curve and time-resolved photoresponse of the photodetector were measured using Keithley 2450 source meter with 405 nm incident light. The square light pulse signal used in the time-resolved photoresponse measurement is generated by driving the LED through WF1946B multifunction synthesizer.

Conflicts of interest

There are no conflicts to declare.

Data availability

The data supporting the findings of this study are available from the corresponding author upon reasonable request.

Supplementary information (SI): additional device characterization data after 8 days of aging, including *I–V* characteristics under different light intensities and the corresponding photocurrent, responsivity, gain, and detectivity analyses. See DOI: https://doi.org/10.1039/d5ra09159d.

Acknowledgements

This work was supported by the Natural Science Foundation of Shandong Province (No. ZR2023QA032), the Innovation Capacity Enhancement Project for Technology-Based SMEs (No. 2025TSGCCZZB0762).

Notes and references

1 V. Laxmi, Y. Tu, D. Tyagi, P. K. Nayak, Y. Tian and W. Zhang, *Nanoscale*, 2025, **17**, 11246–11274.
2 Z. Liu, R. Wang, J. Han, T. Chen, Z. Deng, Y. Sun, Y. Zhao and A. Chen, *Adv. Funct. Mater.*, 2025, **35**, 2424645.
3 C. Ling, C. Rong, B. Men, J. Wang, J. Sun, T. Zhang, L. Zhang, T. Guo, P. Zhou and W. Liu, *Adv. Healthcare Mater.*, 2025, **14**, 2402507.
4 R. Guan, H. Xu, Z. Lou, Z. Zhao and L. Wang, *Advanced Science*, 2024, **11**, 2402530.
5 Q. Wang, H. Wang, M. Sun, R. Xue, M. Ning, S. li, P. Chen and Z. Li, *Opt. Mater.*, 2023, **145**, 114408.
6 S. M. Koepfli, M. Baumann, Y. Koyaz, R. Gadola, A. Güngör, K. Keller, Y. Horst, S. Nashashibi, R. Schwanninger and M. Doderer, *Science*, 2023, **380**, 1169–1174.
7 F. Cao, L. Liu and L. Li, *Mater. Today*, 2023, **62**, 327–349.
8 Y. Ke, L. Yuan, W. Xu, Y. Hu, Q. Hao, J. Liu, J. Zhu, Y. Tu, Q. Zhang and W. Zhang, *Adv. Opt. Mater.*, 2025, **13**, 2402226.
9 J. Han, Z. Fu, J. Wei, S. Han, W. Deng, F. Hu, Z. Wang, H. Zhou, H. Yu and J. Gou, *Light: Sci. Appl.*, 2025, **14**, 362.
10 H. Liang, J. Zhang, X. Zhao, Y. Ye, X. Liu, L. Li, G. Yang and J. Huang, *Small*, 2025, 2501140.
11 X. Lin, H. Deng, Y. Jia, Z. Wu, Y. Xia, X. Wang, S. Chen, Y. Cheng, Q. Zheng, Y. Lai and S. Cheng, *ACS Appl. Mater. Interfaces*, 2022, **14**, 12385–12394.
12 B. Yang, P. Guo, D. Hao, Y. Wang, L. Li, S. Dai and J. Huang, *Sci. China Mater.*, 2022, **66**, 716–723.
13 J. Yang, W. Wang, C. Bao, W. Huang and J. Wang, *Matter*, 2025, **8**, 102207.
14 B. L. Paredes, H. Araújo, F. Froborg, N. Marangou, I. Olcina, T. Sumner, R. Taylor, A. Tomás and A. Vacheret, *Astropart. Phys.*, 2018, **102**, 56–66.
15 Y. Wang, F. Song, Y. Yuan, J. Dang, X. Xie, S. Sun, S. Yan, Y. Hou, Z. Lou and X. Xu, *J. Phys. Chem. Lett.*, 2021, **12**, 2133–2141.
16 J. Hou, W. Li, H. Zhang, S. Sidhik, J. Fletcher, I. Metcalf, S. B. Anantharaman, X. Shuai, A. Mishra and J.-C. Blancon, *Nat. Synth.*, 2024, **3**, 265–275.
17 Y. Wang, J. Liu, Y. Liu, S. Li, X. Xu and Z. Lou, *J. Mater. Chem. C*, 2024, **12**, 10267–10329.
18 Y. Tian, Y. Li, C. Hu, Y. Yang, D. Chen and G. Shen, *ACS Appl. Mater. Interfaces*, 2023, **15**, 13332–13342.
19 Y. Li, J. Zhou, Y. Tian, Z. Wei and G. Shen, *Small Methods*, 2023, **8**, 2300026.
20 G. Ma, Y. Hou, Z. Luo, J. Wu, Y. Miao, C. Yang, X. Wang, F. Zheng, S. Shafique and F. Zhao, *Small*, 2024, **20**, 2405820.
21 R. Xing, P. Shi, D. Wang, Z. Wu, Y. Ge, Y. Xing, L. Wei, S. Yan, Y. Tian, L. Bai and Y. Chen, *ACS Appl. Mater. Interfaces*, 2022, **14**, 40093–40101.
22 Z. Liu, Z. Liu, Q. Sun, T. Zhang, H. Yu, X. Zhang, L. Dai, G. Liao, Y. Shen, X.-L. Zhang, J. Zhu and M. Wang, *J. Mater. Chem. C*, 2022, **10**, 7147–7153.
23 N. Nishimura, H. Kanda, R. Katoh, A. Kogo and T. N. Murakami, *J. Mater. Chem. A*, 2024, **12**, 15631–15640.
24 L. Spee, J. Konietzka and F. Münzer, *J. Phys. Chem. Lett.*, 2025, **16**, 11566–11574.
25 J. Duan, J. Li, G. Divitini, D. Cortecchia, F. Yuan, J. You, S. Liu, A. Petrozza, Z. Wu and J. Xi, *Adv. Mater.*, 2024, **36**, 2403455.
26 Y. Zhang, E. Han, B. W. Zhang, J. Peng, J. Sun, S.-M. Lee, M. Xiao, J.-H. Yun and L. Wang, *Nano Energy*, 2024, **132**, 110368.
27 A. Fieramosca, R. Mastria, K. Dini, L. Dominici, L. Polimeno, M. Pugliese, C. T. Prontera, L. De Marco, V. Maiorano and F. Todisco, *Nano Lett.*, 2024, **24**, 8240–8247.
28 C. Xie, H. Yu, C. Li, C. Fu, L. Yang, W. Yang and Z. Huang, *J. Phys. Chem. Lett.*, 2025, **16**, 7929–7936.
29 K. Li, F. Wu, X. Li, B. Li, Z. Sun, X. Wang, X. Liu and J. Luo, *Small*, 2025, **21**, 2409544.
30 C. Zhang, H. Xiao, Q. Guan, T. Zhu, L. Liang, R. Li, H. Ye, X. Niu and J. Luo, *J. Mater. Chem. C*, 2023, **11**, 5116–5122.
31 S. Kumar, J. Jagielski, S. Yakunin, P. Rice, Y.-C. Chiu, M. Wang, G. Nedelcu, Y. Kim, S. Lin and E. J. Santos, *ACS Nano*, 2016, **10**, 9720–9729.

32 H. Takagi, H. Kunugita and K. Ema, *Phys. Rev. B Condens. Matter*, 2013, **87**, 125421.
33 M. Cui, C. Qin, Y. Jiang, S. Zhang, C. Sun, M. Yuan, Y. Yang and Y. Liu, *Photon. Res.*, 2024, **12**, 563–570.
34 H. Long, X. Peng, J. Lu, K. Lin, L. Xie, B. Zhang, L. Ying and Z. Wei, *Nanoscale*, 2019, **11**, 21867–21871.
35 R. Shimono, R. Nishikubo, M. Pylnev, F. Ishiwari, A. Wakamiya and A. Saeki, *ACS Appl. Energy Mater.*, 2023, **6**, 9381–9389.
36 Y. Tabuchi, K. Asai, M. Rikukawa, K. Sanui and K. Ishigure, *J. Phys. Chem. Solids*, 2000, **61**, 837–845.
37 Y.-L. Ma, J.-Z. Liu, K. Wang, S.-Y. Wang, S.-D. Wu, C.-Q. Wang, Q. Wang and H.-L. Zhang, *J. Phys. Chem. Lett.*, 2025, **16**, 8465–8473.
38 Q. Shang, Y. Wang, Y. Zhong, Y. Mi, L. Qin, Y. Zhao, X. Qiu, X. Liu and Q. Zhang, *J. Phys. Chem. Lett.*, 2017, **8**, 4431–4438.
39 R. Guo, Z. Zhu, A. Boulesbaa, F. Hao, A. Puretzky, K. Xiao, J. Bao, Y. Yao and W. Li, *Small Methods*, 2017, **1**, 1700245.
40 L. Zhang, L. Wu, K. Wang and B. Zou, *Advanced Science*, 2019, **6**, 1801628.
41 W. S. Yang, B.-W. Park, E. H. Jung, N. J. Jeon, Y. C. Kim, D. U. Lee, S. S. Shin, J. Seo, E. K. Kim and J. H. Noh, *Science*, 2017, **356**, 1376–1379.
42 Y. Zhang, Y. Liu, Z. Xu, H. Ye, Q. Li, M. Hu, Z. Yang and S. Liu, *J. Mater. Chem. C*, 2019, **7**, 1584–1591.
43 X. Xu, Y.-M. Xie, Y. Ma, M. Li, C. Ma, C.-S. Lee and S.-W. Tsang, *Sol. RRL*, 2019, **3**, 1900140.
44 D. Liang, Y. Peng, Y. Fu, M. J. Shearer, J. Zhang, J. Zhai, Y. Zhang, R. J. Hamers, T. L. Andrew and S. Jin, *ACS Nano*, 2016, **10**, 6897–6904.
45 J. Li, J. Wang, J. Ma, H. Shen, L. Li, X. Duan and D. Li, *Nat. Commun.*, 2019, **10**, 806.
46 Y. Liu, H. Ye, Y. Zhang, K. Zhao, Z. Yang, Y. Yuan, H. Wu, G. Zhao, Z. Yang and J. Tang, *Matter*, 2019, **1**, 465–480.
47 Z. Tan, Y. Wu, H. Hong, J. Yin, J. Zhang, L. Lin, M. Wang, X. Sun, L. Sun, Y. Huang, K. Liu, Z. Liu and H. Peng, *J. Am. Chem. Soc.*, 2016, **138**, 16612–16615.
48 J. Di, H. Li, L. Chen, S. Zhang, Y. Hu, K. Sun, B. Peng, J. Su, X. Zhao and Y. Fan, *Research*, 2022, **2022**, 9768019.
49 C.-H. Lin, B. Cheng, T.-Y. Li, J. R. D. Retamal, T.-C. Wei, H.-C. Fu, X. Fang and J.-H. He, *ACS Nano*, 2018, **13**, 1168–1176.
50 J. Seo, Y. J. Kim and H. Yoo, *Micromachines*, 2022, **13**, 2089.
51 P. Calado, A. M. Telford, D. Bryant, X. Li, J. Nelson, B. C. O'Regan and P. R. Barnes, *Nat. Commun.*, 2016, **7**, 13831.
52 Y. Liu, N. Borodinov, M. Lorenz, M. Ahmadi, S. V. Kalinin, A. V. Ievlev and O. S. Ovchinnikova, *Advanced Science*, 2020, **7**, 2001176.
53 P. Guo, J. Wang, X. Shen, Q. Lv, X. Li, Z. Xu, S. Han, Y. Bian, Y. Meng and L. Yang, *Nano Res.*, 2025, **18**, 94907347.
54 P. Li, W. Huang, W. Xu, X. Wei, Y. Chen, F. Meng, W. Deng and J. Liu, *Adv. Opt. Mater.*, 2022, **11**, 2201876.
55 H. Lu, W. Tian, F. Cao, Y. Ma, B. Gu and L. Li, *Adv. Funct. Mater.*, 2016, **26**, 1296–1302.
56 Y. Wang, Y. Tang, J. Jiang, Q. Zhang, J. Sun, Y. Hu, Q. Cui, F. Teng, Z. Lou and Y. Hou, *J. Mater. Chem. C*, 2020, **8**, 5399–5408.
57 L. Min, Y. Zhou, H. Sun, L. Guo, M. Wang, F. Cao, W. Tian and L. Li, *Light: Sci. Appl.*, 2024, **13**, 280.
58 W. Peng, J. Yin, K. T. Ho, O. Ouellette, M. De Bastiani, B. Murali, O. El Tall, C. Shen, X. Miao, J. Pan, E. Alarousu, J. H. He, B. S. Ooi, O. F. Mohammed, E. Sargent and O. M. Bakr, *Nano Lett.*, 2017, **17**, 4759–4767.